PNAS RESEARCH ARTICLE | CHEMISTRY

Solvent selection criteria for temperature-resilient lithium–sulfur batteries

Guorui Cai[a], John Holoubek[a], Mingqian Li[b], Hongpeng Gao[a], Yijie Yin[c], Sicen Yu[c], Haodong Liu[a], Tod A. Pascal[a,b,c,d], Ping Liu[b,c,d], and Zheng Chen[a,b,c,d,1]

Edited by Yi Cui, Stanford University, Stanford, CA; received January 12, 2022; accepted April 19, 2022 by Editorial Board Member Peter J. Rossky

All-climate temperature operation capability and increased energy density have been recognized as two crucial targets, but they are rarely achieved together in rechargeable lithium (Li) batteries. Herein, we demonstrate an electrolyte system by using monodentate dibutyl ether with both low melting and high boiling points as the sole solvent. Its weak solvation endows an aggregate solvation structure and low solubility toward polysulfide species in a relatively low electrolyte concentration (2 mol L^{-1}). These features were found to be vital in avoiding dendrite growth and enabling Li metal Coulombic efficiencies of 99.0%, 98.2%, and 98.7% at 23 °C, −40 °C, and 50 °C, respectively. Pouch cells employing thin Li metal (50 μm) and high-loading sulfurized polyacrylonitrile (3.3 mAh cm^{-2}) cathodes (negative-to-positive capacity ratio = 2) output 87.5% and 115.9% of their room temperature capacity at −40 °C and 50 °C, respectively. This work provides solvent-based design criteria for a wide temperature range Li-sulfur pouch cells.

lithium–sulfur batteries | temperature resilience | electrolytes | solvent selection | ion solvation

Significance

High-energy density of rechargeable energy storage systems capable of stable cycling at both extremely low (< −30°C) and high (> 45°C) temperature conditions are highly desired but intrinsically difficult to design. Here we present solvent-based design criteria using a monodentate ether solvent as the model for all-climate temperature working pouch cells. These results will promote the future practical application of low-cost lithium metal batteries with a high theoretical capacity and earth-abundant electrode materials (e.g., sulfur and sulfurized polyacrylonitrile).

Lithium (Li) secondary batteries have received widespread attention due to their intrinsically high energy density, yet their operation is typically constrained to moderate temperature conditions (0 °C < T < 40 °C). The ultralow (< −30 °C) temperatures pose sluggish kinetics and thus lead to a low room–temperature capacity retention (1–8), while the increased parasitic reactivity at elevated (> 45 °C) temperatures leads to poor cycling performance (9–11). Improved performance at either temperature extreme is typically accomplished via engineering of the electrolyte; however, optimization of both high- and low-temperature performance is rarely demonstrated simultaneously due to their unrelated and often opposing design constraints.

External battery warming/cooling systems are typically applied to ensure that batteries operate in an optimal temperature range, wherein additional devices inevitably reduce the energy density and also increase the cost of battery systems (12). To get rid of the battery thermal management systems, it would be a wise choice to increase the temperature tolerance of the electrolyte itself. Although great progress on the optimization of Li–ion battery (LIB) performance has been achieved, the limited theoretical graphite capacity of 372 mAh g^{-1} renders LIBs unable to conceivably achieve 500 Wh kg^{-1} (13). To raise the baseline energy density of Li batteries, significant effort has been focused on the employment of Li metal (13–17). In addition, low-cost elemental sulfur (S), with a theoretical energy density of 2,600 Wh kg^{-1}, has also received attention as a next-generation cathode material (18–23). It can be expected that the increased baseline capacity of both anode and cathode will raise the final energy density under extreme conditions.

However, Li metal anodes are known to encounter poor cycling stability and low Coulombic efficiency (CE) due to the high reactivity of metallic Li and high volume change during cycling paired with undesirable parasitic reactions involving soluble polysulfide (PS) species during the cycling (18–23). In addition, elemental S cathodes encounter limitations such as the low utilization of active S and poor cycling performance, caused by the electronically insulating nature of S and their products Li_2S_2/Li_2S, as well as the aforementioned shuttling of soluble PS intermediates to the Li anode. The above issues are expected to be exacerbated under extreme temperatures. At low temperatures, the poor ionic conductivity and increased viscosity of the electrolyte, as well as sluggish charge transfer kinetics on both the anode and the cathode, reduce overall power density and serve to reduce cycle life due to the poor CE of Li cycling (24–29). At high temperatures, accelerated parasitic reactions between the electrolyte and electrodes and increased PS solubility reduce cycle life as well (30). Some of these deficits can be circumvented by replacing S with sulfurized polyacrylonitrile (SPAN), which can be prepared by a facile thermal treatment of low-cost and earth-abundant materials of S with PAN. Benefiting from covalent bonding between short-chain S and

Author affiliations: [a]Department of NanoEngineering, University of California, San Diego, La Jolla, CA 92093; [b]Program of Chemical Engineering, University of California, San Diego, La Jolla, CA 92093; [c]Program of Materials Science and Engineering, University of California, San Diego, La Jolla, CA 92093; and [d]Sustainable Power and Energy Center, University of California, San Diego, La Jolla, CA 92093

Author contributions: G.C. and Z.C. designed research; G.C. performed research; J.H., M.L., H.G., Y.Y., S.Y., H.L., T.A.P., and P.L. contributed new reagents/analytic tools; G.C., J.H., and Z.C. analyzed data; and G.C., J.H., and Z.C. wrote the paper.

The authors declare no competing interest.

This article is a PNAS Direct Submission. Y.C. is a guest editor invited by the Editorial Board.

Copyright © 2022 the Author(s). Published by PNAS. This article is distributed under Creative Commons Attribution-NonCommercial-NoDerivatives License 4.0 (CC BY-NC-ND).

[1]To whom correspondence may be addressed. Email: zhengchen@eng.ucsd.edu.

This article contains supporting information online at http://www.pnas.org/lookup/suppl/doi:10.1073/pnas.2200392119/-/DCSupplemental.

Published July 5, 2022.

PAN within the conductive SPAN host, a solid-to-solid conversion mechanism is applied to SPAN during the charging/discharging process that does not theoretically rely on PS (31–36). However, ester-based electrolytes are generally required to ensure the stability of the covalently bonded, redox-active S species, which generally demonstrate poor compatibility with the Li metal, especially at ultralow temperatures (26). Electrolytes based on ether electrolytes typically display significantly improved Li metal performance, but few of these systems are simultaneously compatible with SPAN cathodes due to undesired PS dissolution (34, 35).

Recently, our group demonstrated that diethyl ether (DEE) can be employed as a viable solvent for ultralow-temperature (−60 °C) Li metal batteries (LMBs) due to its strong Li^+/anion interaction and weak Li^+–solvent binding, which induces ion pairing in solution (29). It was concluded that these 2 factors produce a facile Li^0/Li^+ charge transfer due to their influence on interphasial dynamics and ion desolvation. Despite the unprecedented low-temperature Li metal cyclability of this DEE system, its high volatility (vapor pressure, P_{vap} = 0.7 atm) and low boiling point (T_b = 35 °C) prohibited its application at high temperatures. Hence, the impact of these factors on elevated temperature performance has yet to be investigated. So far, electrolytes that are compatible with both an Li metal and an S cathode and retain high energy density and stable cycling at a wide temperature range remain to be developed.

To achieve this, we developed an electrolyte for wide-temperature Li–S batteries with the monodentate dibutyl ether (DBE) as the sole solvent and lithium bis(fluorosulfonyl)imide (LiFSI) as the salt (Fig. 1*A*). We found that similar to previously studied monodentate ether electrolytes, DBE provides a highly ion–paired solvation structure at a low salt concentration due to its weak Li^+–solvent binding interactions. However, unlike smaller monodentate solvents, DBE provides both low melting and high boiling points. These advantageous wide-temperature properties allow the advantages of the ion-paired solvation environment to simultaneously improve low-temperature kinetics while forming inorganic interphases that passivate the electrodes during high-temperature cycling. Specifically, high-Li metal CEs of 99.0%, 98.2%, and 98.7% CE at 23 °C, −40 °C, and 50 °C, respectively, were developed in addition to homogenous Li metal deposition morphology. The reduced PS solubility of this electrolyte also resulted in superior long-term cycling performance under ambient conditions with a capacity fade of 0.06% per cycle over 200 cycles in Li//SPAN cells with a loading of ∼1.2 mAh cm^{-2} SPAN. When cycling the cells at extreme conditions, Li//SPAN pouch cells with twofold excess Li metal and a high cathode loading of ∼3.3 mAh cm^{-2} delivered specific capacities of 479 mAh g^{-1}, 419 mAh g^{-1}, and 555 mAh g^{-1} at 23°C, −40°C, and 50 °C, respectively.

Results

Selection of solvents. For the electrolyte design of LMBs, it has been recognized that ethers, which offer a higher lowest unoccupied molecular orbital energy than esters, exhibit promise toward achieving superior compatibility with Li metal anodes (37–40). Among the ether solvents, 1,3-dioxolane (DOL), dimethoxyethane (DME), diglyme (G2), triglyme, and other large-sized molecules have been used for Li–S batteries due to their high electrochemical stability toward both the cathode and the anode (41–43). Despite their relatively high ionic conductivity, recent work showed that typical ether-based electrolytes (e.g., DOL/DME system) encountered dendritic Li metal growth at subzero temperatures (44). While the underlying mechanism of this behavior under extreme conditions is still unclear, it is likely attributed to the significantly increased charge–transfer resistance at low temperatures. Our previous work showed that DEE can partially address this limitation by providing facile desolvation kinetics. Although it was demonstrated as a model solvent for ultralow temperatures, it is not stable at elevated temperatures due to its high volatility (29). As shown in the supporting movie (Movie S1), a drop of DEE rapidly evaporates under ambient conditions. These safety concerns also render it unsuitable for future practical applications, especially for pouch cells.

Compared to the monodentate ether DEE, multidentate ethers such as DOL (T_b = 75 °C, P_{vap} = 0.092 atm), DME (T_b = 85 °C, P_{vap} = 0.063 atm), and G2 (T_b = 162 °C, P_{vap} = 0.004 atm) show a higher boiling point and lower vapor pressure. However, stronger Li^+–solvent binding is produced by these solvents due to the increase of oxygen units in each ether molecule (i.e., chelated effects) (38, 40), which results in high impedance for charge transfer at low temperatures. Therefore, it is not a viable approach to improve high-temperature performance by using more complex multidentate ether solvents by scarifying the low-temperature performances. In addition, the increased solubility of PS poses dramatically reduced cycling performance due to parasitic reactions at both the anode and the cathode, especially at high temperatures.

In this work, we leveraged our understanding of the advantageous solvation structures inherent to monodentate ethers from our previous DEE work to design an electrolyte for wide-temperature LMBs. To balance the physicochemical properties at both ultralow and high temperatures, DBE ($CH_3(CH_2)_3O(CH_2)_3CH_3$), with low melting (−98 °C) and high boiling (T_b = 142 °C) points as well as low vapor pressure (P_{vap} = 0.006 atm), was selected as the solvent. In order to evaluate the promise of DBE for wide-temperature electrolytes, 2 M LiFSI in DBE was employed in order to balance the ion pairing found at an elevated salt concentration (≥ 2 M) and low viscosity (≤ 2 M) for facile Li^+ diffusion. To investigate the effect of solvent chemistry on LMB performance in extreme environments, other ether-based systems (e.g., DME and G2) with an incrementally increased number of ether oxygens per molecule were also prepared with an identical LiFSI concentration (2 M) for the comparison, considering their ostensibly acceptable physicochemical properties (37–40). To preliminarily confirm the hypothesized electrolyte behavior at extreme conditions, the systems of interest were stored at −60 °C overnight. As shown in *SI Appendix*, Fig. S1, both 2 M LiFSI DME and 2 M LiFSI G2 systems were found to freeze whereas 2 M LiFSI DBE systems remained in a liquid phase, representative of the low melting point of the monodentate ether compared to conventional multidentate ethers.

Li metal in selected electrolytes. To investigate the compatibility of selected electrolytes with Li metal at a wide temperature range, Li//Cu cells were assembled by using 2 M LiFSI in DBE, DME, and G2, respectively. The accurate method proposed by Adams et al. (45) was employed to determine the Li plating/striping CE. As presented in Fig. 1 *B* and *C*, although the DBE system only exhibited a slightly increased CE compared with that of DME and G2 systems at room temperatures (99.0% vs. 98.9% and 96.7%), the advantage became more obvious at an elevated temperature (98.7% vs. 91.3% and 87.1%). In addition, the DME and G2 systems posed unstable voltage curves when the temperature is reduced to zero (Fig. 1*D*). By sharp

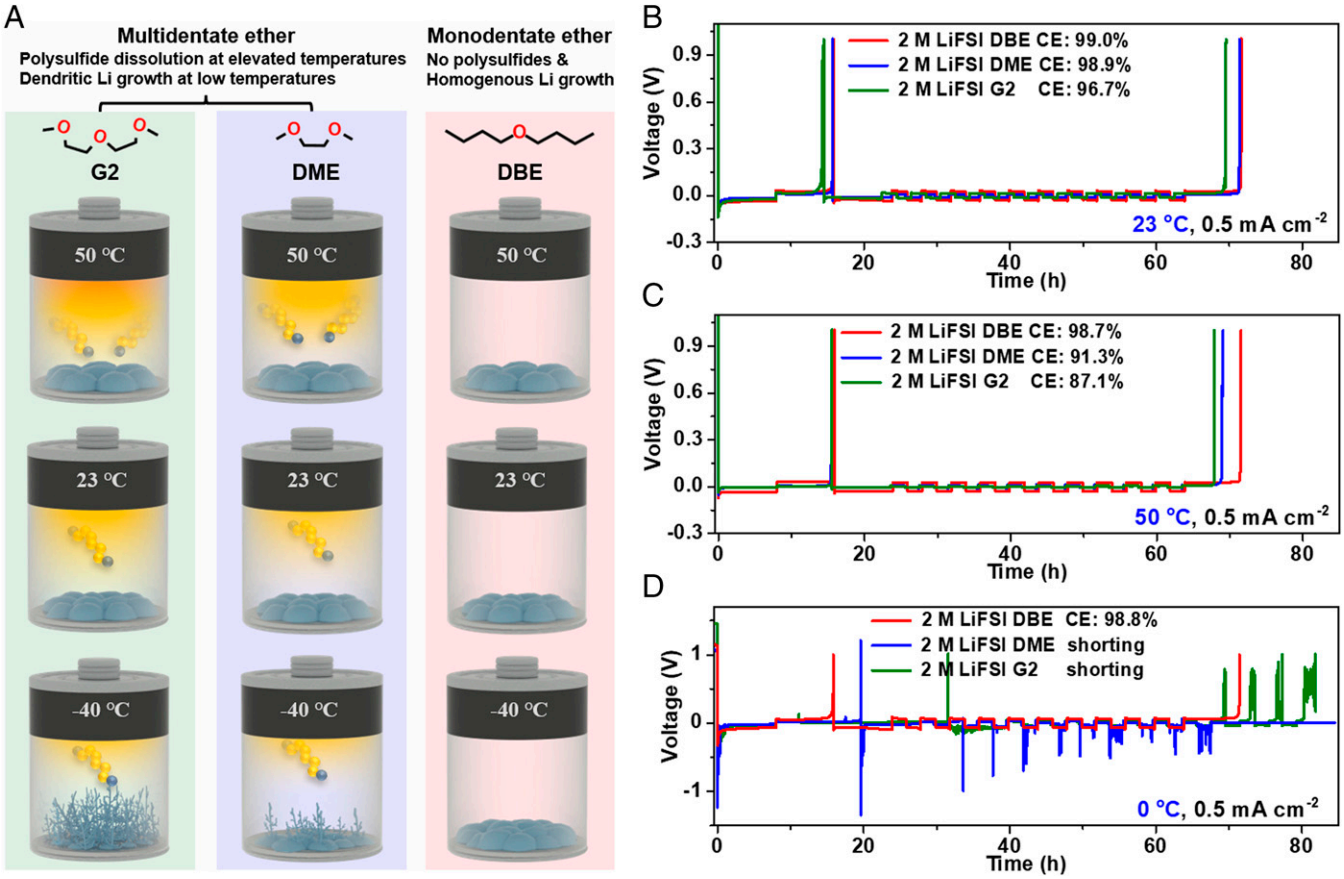

Fig. 1. Li metal plating/stripping in a wide temperature range. (*A*) Schematic showing the Li plating and S conversion behaviors of multidentate (DME, G2) and monodentate ether (DBE) systems under a wide temperature range. An increased PS species shuttle of SPAN cathodes at elevated temperatures and dendritic growth of Li metal under subzero temperatures in a conventional multidentate ether electrolyte system, in which the monodentate DBE electrolyte system does not share the same trend. CE-determined curves for the electrolytes of 2 M LiFSI DBE, 2 M LiFSI DME, and 2 M LiFSI G2 at (*B*) 23 °C, (*C*) 50 °C, and (*D*) 0 °C, respectively.

contrast, the DBE system retained smooth plating/stripping voltage curves with a high CE of 98.2% even at −40 °C (*SI Appendix*, Fig. S2). The long-term cycling further indicated that the DME and G2 electrolyte systems exhibited fluctuated CE curves even under ambient conditions (*SI Appendix*, Fig. S3). On the contrary, we found that the DBE system achieved stable and reversible Li metal cycling over a wide temperature range with high average CEs of 98.8%, 98.0%, and 96.2% at 23 °C, −40 °C, and 50 °C, respectively, after 100 cycles (*SI Appendix*, Figs. S3 and S4).

To further evaluate the Li deposition behavior at ultralow temperatures, an attempt at depositing 4 mAh cm^{-2} Li metal was carried out on Cu foil with a current density of 0.5 mA cm^{-2} at 0 °C. The Li//Cu cells with 2 M LiFSI DME and 2 M LiFSI G2 showed fluctuating voltage curves, indicating a soft-shorting issue (29). Nevertheless, the cell with 2 M LiFSI DBE did not share this same trend (Fig. 2 *A*–*C*). To confirm this soft shorting, the cells after Li deposition steps were disassembled and the macroscopic morphology of the plated Li was compared based on their optical photographs. As exhibited by the insets of Fig. 2 *A*–*C* (*Left*), a smooth Li disk with a similar size and morphology to the Li counter was deposited on the Cu foil in 2 M LiFSI DBE. However, only isolated Li deposits were produced on the Cu foil in 2 M LiFSI DME and 2 M LiFSI G2, further indicating that shorting played a role. To gain more detailed information about the Li metal plating behavior, we collected their microscopic features via scanning electron microscopy (SEM). The SEM images of deposited Li metal revealed a temperature-dependent Li morphology (Fig. 2 *A*–*C*, *Right*, insets), in which porous and fibrous Li was deposited in DME and G2 systems at subzero temperatures. On the contrary, the Li deposited in 2 M LiFSI DBE still maintained a chunk morphology regardless of the temperature, although it was accompanied by decreased chunk sizes with the drop in temperature (*SI Appendix*, Fig. S5).

To understand the underlying mechanism of the DBE electrolyte system as a wide-temperature electrolyte, the conductivities of each electrolyte were measured from −40 °C to 50 °C (Fig. 2*D*). Interestingly, the electrolytes employing DME and G2 maintained consistently higher ionic conductivity at all measured temperatures than that of the DBE system. Therefore, the deviation of Li metal performance at low temperatures between the mono- and multidentate ether electrolytes cannot be attributed to the reduction of bulk ion transfer in the electrolytes at reduced temperatures. To investigate their kinetic behavior, we conducted electrochemical impedance spectroscopy (EIS) at multiple temperatures. At ambient and high-temperature conditions (*SI Appendix*, Fig. S6 and Fig. 2*E*), the DBE electrolyte exhibited increased bulk impedance compared to the DME and G2 electrolytes (24 Ω for DBE vs. 5 Ω and 10 Ω for DME and G2, respectively, at 23 °C; 19 Ω vs. 4 Ω and 4 Ω at 50 °C), whereas slightly reduced charge transfer resistances were shown in the DBE system (25 Ω vs. 90 Ω and 41 Ω at 23 °C; 6 Ω vs. 10 Ω and 16 Ω at 50 °C). This deviation became more obvious at subzero temperatures, where DME and G2 electrolytes exhibited significantly increased charge transfer resistance (Fig. 2*F*). This result indicates that

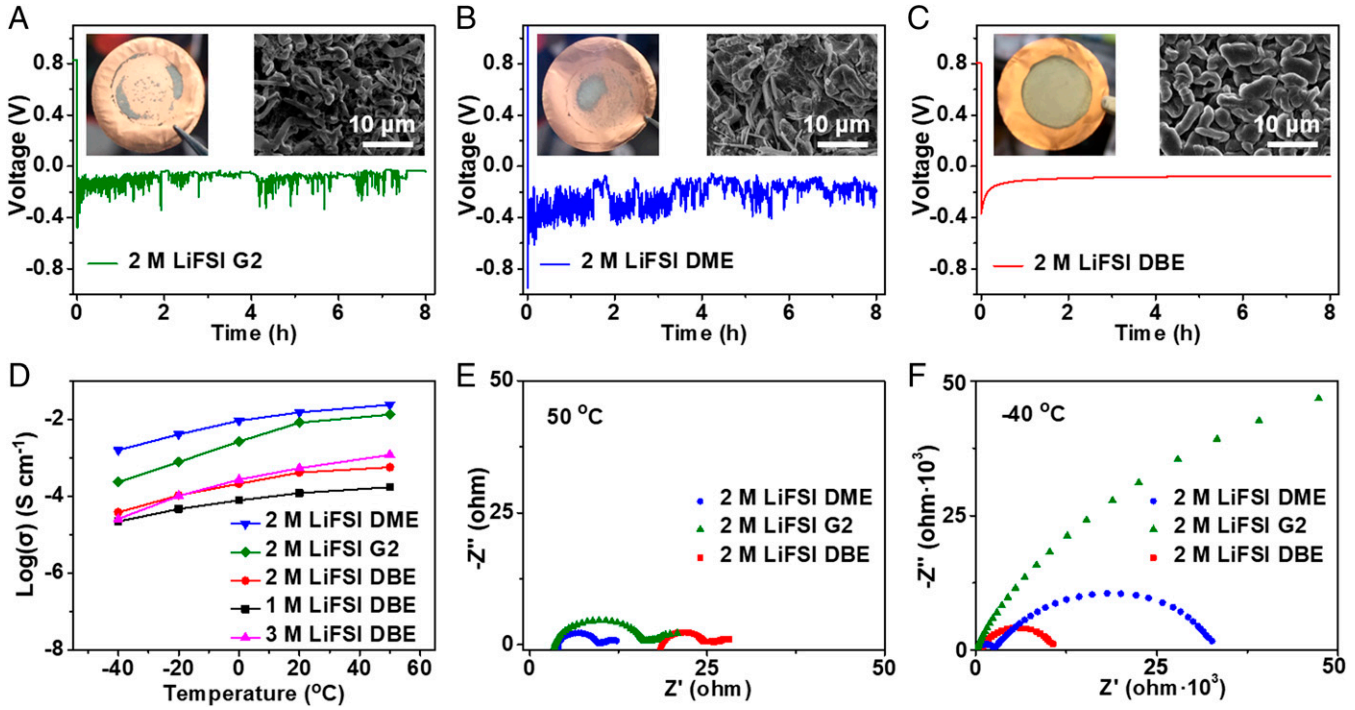

Fig. 2. Plated Li metal, ionic conductivity, and electrochemical impedance in selected electrolytes. (*A–C*) Li deposition profiles of 4 mAh cm^{-2} at 0.5 mA cm^{-2} in the electrolyte systems of (*A*) 2 M LiFSI G2, (*B*) 2 M LiFSI DME, and (*C*) 2 M LiFSI DBE at 0 °C. Insets in *A–C* are (*Left*) optical photos of deposited Li on Cu foil, in which the sparse and reduced amount of plated Li in the DME and G2 systems are caused by the shorting events, and (*Right*) SEM images of deposited Li metal (Scale bars, 10 μm). (*D*) Ionic conductivity of 2 M LiFSI in G2 and DME, as well as 1 M, 2 M, and 3 M LiFSI in DBE at a wide temperature range. EIS impedance plots of Li//Li symmetric cells with 2 M LFSI dissolved in DBE, DME, and G2 after cycling at (*E*) 50 °C and (*F*) −40 °C for 5 runs, respectively.

the charge transfer impedance poses no noticeable influence on the high-temperature performance while it dominates the low-temperature Li metal performance, in which the DBE electrolyte is preferable to the DME and G2 systems.

Solvation structures. The desolvation penalty faced by Li^+ ions in solution has been hypothesized to be the defining factor in low-temperature charge transfer (4, 29). To probe the improved kinetics of the DBE system at low temperatures, the solvation structures of each electrolyte were simulated via classical molecular dynamics (MD). As presented in Fig. 3, the radial distribution functions of Li^+ in 2 M LiFSI DBE indicated that the first Li^+ solvation shell comprises on average 3.1 FSI^- anions and 1.2 DBE solvent molecules, a typical feature of the aggregate (AGG) structure (Fig. 3 *A*, *D* and *E*), which is generally found in high-concentration or localized high-concentration electrolytes (46–48). This structure is generally attributed to the weak interactions between DBE and Li^+ compared to those between multidentate ether solvents and Li^+. On the contrary, the DME with identical LiFSI concentrations was predicted to produce a half–solvent-separated ion pair (SSIP) and half–contact ion pair (CIP) structure with a coordination number of 2.5 DME (0.5 FSI^-) oxygens per Li^+ ion (Fig. 3 *B* and *D* and *E*), while the G2 electrolyte presented an SSIP structure with 1.8 G2 (0 FSI^-) molecules per Li^+ ion (Fig. 3 *C* and *D*), in which the Li^+ ions are primarily coordinated by solvent molecules. The noticeable differences of solvation structures compared with the deviation of Li deposition indicate that the AGG structure in the DBE system may fundamentally define the observed low-temperature performance in this work; a similar phenomenon was previously observed in CIP structures compared with SSIP structures to improve low-temperature kinetics (29).

The solvation structures observed in MD were confirmed via Raman spectroscopy of the selected electrolytes and their components (Fig. 3*F*). The S–N–S bending peak (774 cm^{-1}) of the LiFSI salt presented a significant redshift to approximately 717 cm^{-1} upon dissolution in DME and G2. Considering the conclusions from previously published works that the increased coordination of cation/solvent and the reduced coordination of cation/anion led to a more significant redshift of anion modes, the trends shown by the DME and G2 systems indicate a stronger dissociation of the Li^+/FSI^- interactions that is characteristic of highly solvated structures. On the contrary, the S–N–S bending peak in the DBE system underwent a much smaller shift to only 746 cm^{-1}, indicative of much stronger interactions between Li^+/FSI^-, in agreement with the MD-predicated AGG structures.

The above computational simulation and experimental results suggest that there is more cation/anion binding and less cation/solvent binding in the DBE electrolyte (AGG) compared to those in the DME (half-SSIP and half-CIP) and G2 (SSIP) electrolyte systems. In addition, the monodentate solvent (DBE) with weak solvation ability is expected to endow weak cation/solvent binding compared to those multidentate solvents (DME, G2) with strong solvation ability (29, 38, 40). As a result, the DBE electrolyte system can allow more facile desolvation kinetics than those in the DME and G2 electrolyte systems. Considering that the impedance of the interfacial charge transfer is suggested to be dominated by the Li^+ desolvation process at low-temperature conditions (4, 29), the DME and G2 electrolyte systems may also lead to a sluggish interfacial charge transfer on the Li metal. Therefore, a vastly increased charge–transfer impedance in the DME and G2 electrolyte systems can be found (Fig. 2*F*). The above analysis indicates that the DBE electrolyte system (AGG) can produce more facile desolvation kinetics and interfacial charge transfer than those in the CIP and SSIP solvation structures.

Li–S half-cells. In order to evaluate the promise of the DBE electrolyte for Li–S batteries, the PS solubility in each solvent was

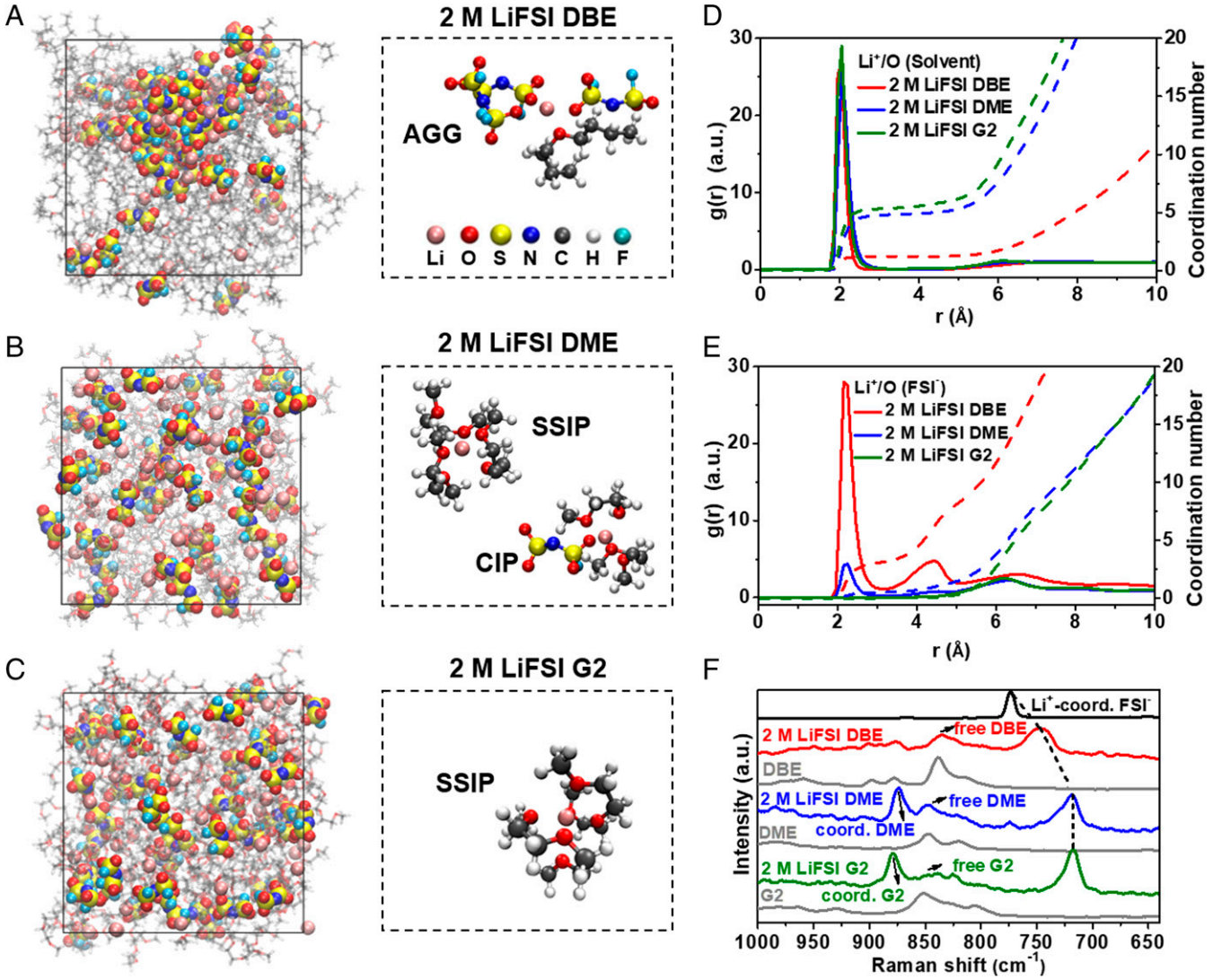

Fig. 3. Computational and experimental analysis of solvation structure. Snapshot and most representative solvation structure extracted from MD simulation for (*A*) 2 M LiFSI DBE, (*B*) 2 M LiFSI DME, and (*C*) 2 M LiFSI G2. (*D* and *E*) Li^+ radial distribution function obtained from MD simulations. (*F*) Raman spectra of selected electrolytes and corresponding components. The arbitrary units are simplified as a.u. in *D*, *E*, and *F*.

tested. Unlike the conventional ether solvents, the DBE solvent exhibited substantially reduced PS solubility (Fig. 4*A*). Based on the above advantage, the low-lost SPAN, which prefers a solid-to-solid conversion (31–36), was selected as the cathode material of wide-temperature Li–S batteries. To investigate this effect on the cycling performance of cathodes at a wide temperature range, half-cells employing a thick Li metal disk as the anode with a moderate mass loading of SPAN (1.2 mAh cm^{-2}) as the cathodes were assembled with the selected electrolytes. As shown in Fig. 4*B*, Li//SPAN half-cells with 2 M LiFSI DBE output 99.8% and 101.6% of their room temperature capacity (552 mAh g^{-1}) at −40 and 50 °C, respectively. After running 200 cycles, only an average capacity fade of 0.06% per cycle could be found in the DBE electrolyte systems at the ambient temperature, in which the DME and G2 electrolytes showed a decay of 0.21% and 0.28% per cycle, respectively (*SI Appendix*, Fig. S7). The advantages of DBE electrolytes were further highlighted when running the cells under −40 °C (Fig. 4*C*), in which no capacity could be delivered in the DME and G2 electrolyte systems caused by their high charge–transfer impedance (Fig. 2*F*) and poor compatibility with Li metal at low temperatures (Fig. 1*D*). When Li//SPAN half-cells were run at an elevated temperature (50 °C), the DME and G2 electrolyte systems underwent faster capacity fading than the DBE electrolyte system, comparing the trends in ambient temperature (Fig. 4*D* and *SI Appendix*, Fig. S7), which can be attributed to the increased solubility of PS and parasitic reactivity at high temperatures (Fig. 4*A*).

Mechanism for temperature-resilient Li–S batteries. To figure out the underlying mechanism for the above performance deviation, the Li//SPAN half-cells cycled at 50 °C were disassembled and the morphology of the Li counter electrodes was examined by the SEM (*SI Appendix*, Fig. S8), where the DME and G2 systems presented rough and porous surfaces, in sharp contrast to the morphology in the Li//Cu cells (*SI Appendix*, Fig. S5 *D* and *E*). After checking the separator in the cycled Li//SPAN cell, we found a light-yellow color in the DME electrolyte system and a more noticeable yellow color in the G2 electrolyte system (*SI Appendix*, Fig. S9), suggesting the accumulation of soluble PS species. In addition, X-ray photoelectron spectroscopy (XPS) spectra of the delithiated SPAN cathodes further indicated the existence of some PS species in the cycled SPAN with the G2 electrolyte system (*SI Appendix*, Fig. S10). The apparent differences between the morphology of plated Li and the color of the separators in the

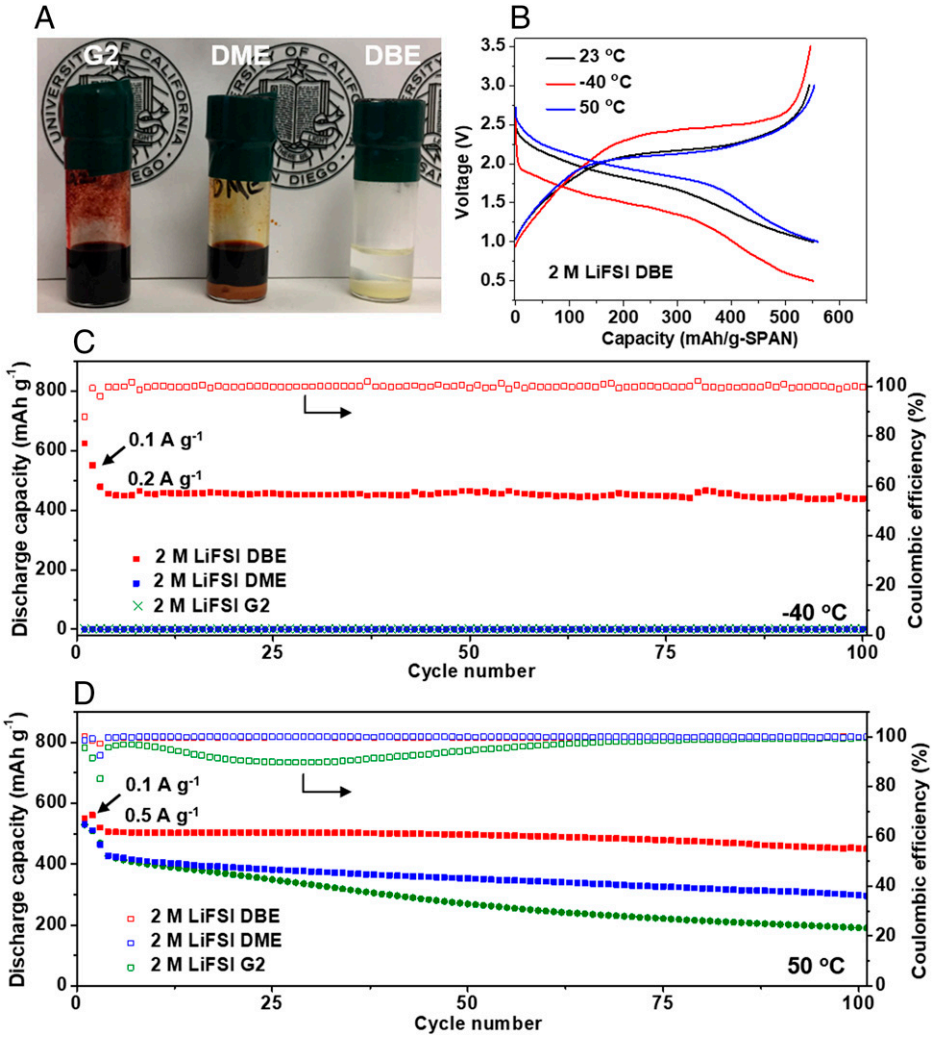

Fig. 4. Li–S half-cell performance at a wide temperature range. (*A*) Photographs of selected solvents to produce 0.25 M Li_2S_6 by dissolving/dispersing stoichiometric amounts of Li_2S and S in selected solvents (from left to right: G2, DME, and DBE) for 2 d. (*B*) Voltage curves of Li//SPAN cells in 2 M LiFSI DBE at 23 °C, −40 °C, and 50 °C with a current density of 0.1 A g^{-1}. Cycling performance of Li//SPAN cells in different electrolytes at (*C*) −40 °C and (*D*) 50 °C.

cycled Li//SPAN cells can be attributed to the shuttling and subsequent reaction of PS with Li metal (Fig. 4*A*) (27, 28). By comparison, the DBE electrolyte presented stable cycling capacity, a clean and pristine white color of the separator, and a smooth Li metal surface at both ambient and high temperatures (Fig. 4*D* and *SI Appendix*, Figs. S5*F* and S8*A*), which indicates that low PS solubility plays an important role in the cycling stability of Li//SPAN half-cells, especially at elevated temperatures. In addition, the DBE electrolyte also delivered a high stable cycling performance when cycled at both 23 °C and -40 °C (Fig. 4*C*). After comparing the voltage curves of Li//SPAN cells at different temperatures, the low-temperature cells presented an obviously increased overpotential compared with those at ambient and high temperatures (Fig. 4*B*). To reveal the underlying reason, 3-electrode cells were assembled by using Li, Li, and SPAN as the reference, counter and working electrodes, respectively. Comparing the individual electrode and the cell voltage, we found that the working electrode exhibited an almost identical voltage curve compared to the full cell regardless of the temperature (*SI Appendix*, Fig. S11 *A–C*). To better compare the overpotential change in each voltage curve at different temperatures, the discharging median voltage at 50 °C and -40 °C relative to 23 °C are shown in *SI Appendix*, Fig. S11*D*. All voltage curves at 50 °C delivered slightly reduced overpotentials compared with those at ambient conditions, attributed to facile kinetics at elevated temperatures. However, they underwent apparently increased overpotentials at -40 °C, in which the working electrode contributed the most in full cells (|ΔV|: 0.39 vs. 0.46 V). These results indicate that the increased overpotential is mainly from the cathode side.

Concentration and anion effect. To gain more information about the effect of ion concentration on the performance of Li–S batteries with DBE electrolytes, we explored the DBE electrolytes with different LiFSI concentrations. Per *SI Appendix*, Fig. S12, the Li//Cu cells employing 1 M LiFSI DBE showed unstable voltage at −40 °C. In addition, the Li//SPAN cells employing this electrolyte presented a more-rapid capacity fade compared to those with 2 M and 3 M concentrations at 50 °C (*SI Appendix*, Fig. S13 and Fig. 4*D*). On the other hand, although it was observed that the 3 M system sustained stable plating/stripping with a high CE of 96.6% at −40 °C in Li//Cu cells (*SI Appendix*, Fig. S12), this system delivered significantly reduced SPAN capacity compared to the 2 M system (*SI Appendix*, Fig. S14). This development may be caused by the increased viscosity of high-concentration electrolytes, which poses a high overpotential for the low-temperature conversion reaction of SPAN cathodes, as shown in the 3-electrode testing (*SI Appendix*, Fig. S11). In addition, the Li//SPAN cells suffered from poor cycling retention at −40 °C

when the conventional ester (1 M $LiPF_6$ EC/DEC 1/1 in vol.) and ether (1 M LiTFSI, 0.2 M $LiNO_3$ DOL/DME 1/1 in vol.) electrolytes were used, despite stable performance at room temperature (*SI Appendix*, Figs. S15 and S16). On the other hand, the high concentration electrolytes (e.g., 4 M LiFSI DBE and 7 M LiTFSI DOL/DME 1/1 in vol.) failed to deliver any capacity at subzero temperatures and presented poor performance under increased current density even at ambient temperature, which can be attributed to their poor wettability (*SI Appendix*, Figs. S17 and S18). The above results further highlight the advantage of the medium-concentration DBE electrolyte, which offers facile Li^+ kinetics in addition to high boiling and low melting points for wide-temperature batteries.

To better understand this concentration effect, we also simulated the solvation structures of different DBE electrolytes via MD (*SI Appendix*, Figs. S19 and S20). Analysis of the radial distribution function (RDF) data revealed that all the above DBE electrolytes displayed ion–pairing structures, while 1 M LiFSI DBE (CIP structures) presented a higher solvent coordination number and less FSI^- anion participation in the solvation shell compared with the 2 M and 3 M systems (AGG structures). This was also observed in the Raman spectra of these electrolytes, in which a reduced redshift from 774 cm^{-1} (S–N–S bending peak of LiFSI salt) to 745 cm^{-1}, 746 cm^{-1}, and 749 cm^{-1} was found with the increase of LiFSI concentration in DBE from 1 M to 2 M and 3 M (*SI Appendix*, Fig. S21), indicating stronger interactions between Li^+ and FSI^- with the increase of the LiFSI concentration. Considering the deviation of Li plating behaviors and their solvation structures in DBE electrolytes with different concentrations, the AGG structures (2 M and 3 M) with a higher ratio of FSI^- in the solvation structure and stronger ion–pairing structures were superior to the CIP structures (1 M) toward the low-temperature Li metal. Notably, the 2 M LiFSI DBE presented a well-balanced performance for both the low- and high-temperature performances.

Apart from the above concentration effects, the possible anion effects toward the battery performances were also evaluated by changing the Li salts. Per *SI Appendix*, Fig. S22, $LiPF_6$ and $LiBF_4$ were found to be insoluble (< 0.1 M) in DBE solvents even after heating at 80 °C overnight. This finding indicates that the weak solvation ability of DBE fails to disassociate the strong binding of Li^+ cations and PF_6^- and BF_4^- anions. Despite that development, 2 M LiTFSI DBE was found to produce an Li metal CE lower than that with LiFSI salt (96.5% vs. 99.0%) at ambient condition. The long-term cycling of Li//Cu cells with a calculated average CE of 94.4% further demonstrated the relatively poor stability in the 2 M LiTFSI DBE electrolyte (*SI Appendix*, Fig. S23). In addition, the Li//Cu cells with 2 M LiTFSI DBE presented a large overpotential and failed to run at −40 °C. The above results further highlight the advantage of LiFSI toward wide-temperature Li batteries.

Li–S pouch cells. To further examine the potential of the DBE electrolyte system toward practical LMBs at a wide temperature range, Li//SPAN pouch cells (size = 5.8 cm * 4.5 cm; negative-to-positive capacity (N/P) ratio = 2; electrolyte = ∼7 μL/mg_{SPAN}) with a high mass loading of ∼3.3 mAh cm^{-2} SPAN were assembled (Fig. 5*A*). Per Movie S2, the pouch cell with a highly volatile electrolyte system (2 M LiFSI DEE) bulged immediately upon exposure to an 80 °C hot plate (Fig. 5*B*, *Left*, inset), while no noticeable change could be found in the pouch cell employing the 2 M LiFSI DBE electrolyte (Fig. 5*B*, *Right*, inset) because of the high boiling point and low volatility of DBE. The electrochemical performance of these pouch cells was also collected at ambient and extreme temperatures. The pouch cells employing 2 M LiFSI DBE delivered a high capacity (479 mAh g^{-1}) and cycling stability over 50 cycles at room temperature (Fig. 5 *C* and 5*D*). After reducing the working temperature to −40 °C, the pouch cell employing DBE still maintained a high capacity (419 mAh g^{-1}). On the contrary, although the pouch cell employing volatile DEE delivered 597 mAh g^{-1} at −40 °C, only 478 mAh g^{-1} could be delivered at an ambient condition, followed by a rapid capacity decay (330 mAh g^{-1} at the fourth cycle) and even failed to charge again (Fig. 5 *D* and *E*). Although Li–S cells at elevated temperatures typically suffer from increased parasitic reactions, the full cells with DBE delivered a high capacity (555 mAh g^{-1}) at 50 °C and could be continuously cycled more than 30 times (Fig. 5*F*), while almost no capacity could be delivered in those with a volatile DEE system due to the evaporation of the volatile electrolyte under elevated temperatures. The above results further suggest the promise of DBE for wide-temperature Li// SPAN batteries.

Discussion

In summary, we have developed a monodentate DBE-based ether electrolyte system for wide-temperature Li–S batteries, which allows scalable pouch cells (∼83 mAh) with limited Li metal (N/P ratio = 2) to be cycled with high-capacity retention at 23 °C, −40 °C, and 50 °C. Apart from both low melting and high boiling points, this ether electrolyte promotes the formation of the AGG type of solvation structures at a relatively low concentration (2 M), which is crucial for facile low-temperature kinetics of Li metals while maintaining a high CE (∼99%) at a wide temperature range from −40 °C to 50 °C. In addition, DBE also poses a low PS solubility, thereby ensuring a high compatibility with both electrodes of Li–S cells, especially at elevated temperatures. This work provides important solvent selection criteria for temperature-resilient LMB to deliver increased energy density even in harsh environments.

Materials and Methods

Electrode preparation. The SPAN powder was synthesized by hand milling of elemental S (Sigma-Aldrich) and PAN (Sigma-Aldrich, Mw = 150,000) in a mass ratio of 4:1. The obtained homogeneous mixture was heated to 450 °C with a ramp rate of 2 °C min^{-1} in a tube furnace and held at 450 °C for 6 h, followed by cooling down to room temperature. The obtained SPAN powder was milled with Super-P by hand to produce a homogeneous mixture, followed by dispersal into an N methyl pyrrolidinone of PVDF (KYNAR 2800) using a Thinky mixer. After being dried at 120 °C under vacuum overnight, the SPAN cathode was obtained. The mass ratio of SPAN:Super-P:PVDF was fixed at 70:15:15. The mass loading of SPAN can be controlled by adjusting the thickness of the slurry during the slurry–casting process. The obtained electrodes have a typical SPAN loading of approximately ∼1.2 mAh cm^{-2} for low-mass loading cells or ∼3.3 mAh cm^{-2} for high-mass loading cells. All the areal capacity loadings of the coin and pouch cells were calculated based on a specific capacity of 600 mAh g^{-1} for SPAN.

CE calculation. The calculation of Li metal CE was based on the accurate CE test popularized by Adams et al. (45). CR-2032–type Li//Cu cells with selected electrolytes and a small-sized Li metal disk (7/16 in, China Energy Lithium Co., 99.9%) was assembled. A 4 mAh cm^{-2} Li was first plated on Cu foil, followed by stripping to 1 V before the testing of CE. Subsequently, another 4 mAh cm^{-2} Li was deposed on Cu foil. Before it was fully stripped to 1 V, a plating and stripping step of 1 mAh cm^{-2} Li was allowed to cycle 10 times. The value of total stripped capacity divided by the total plated capacity was calculated as the CE.

Morphology observation and surface analysis. To evaluate the plated Li metal morphology under selected electrolytes, SEM samples were collected by

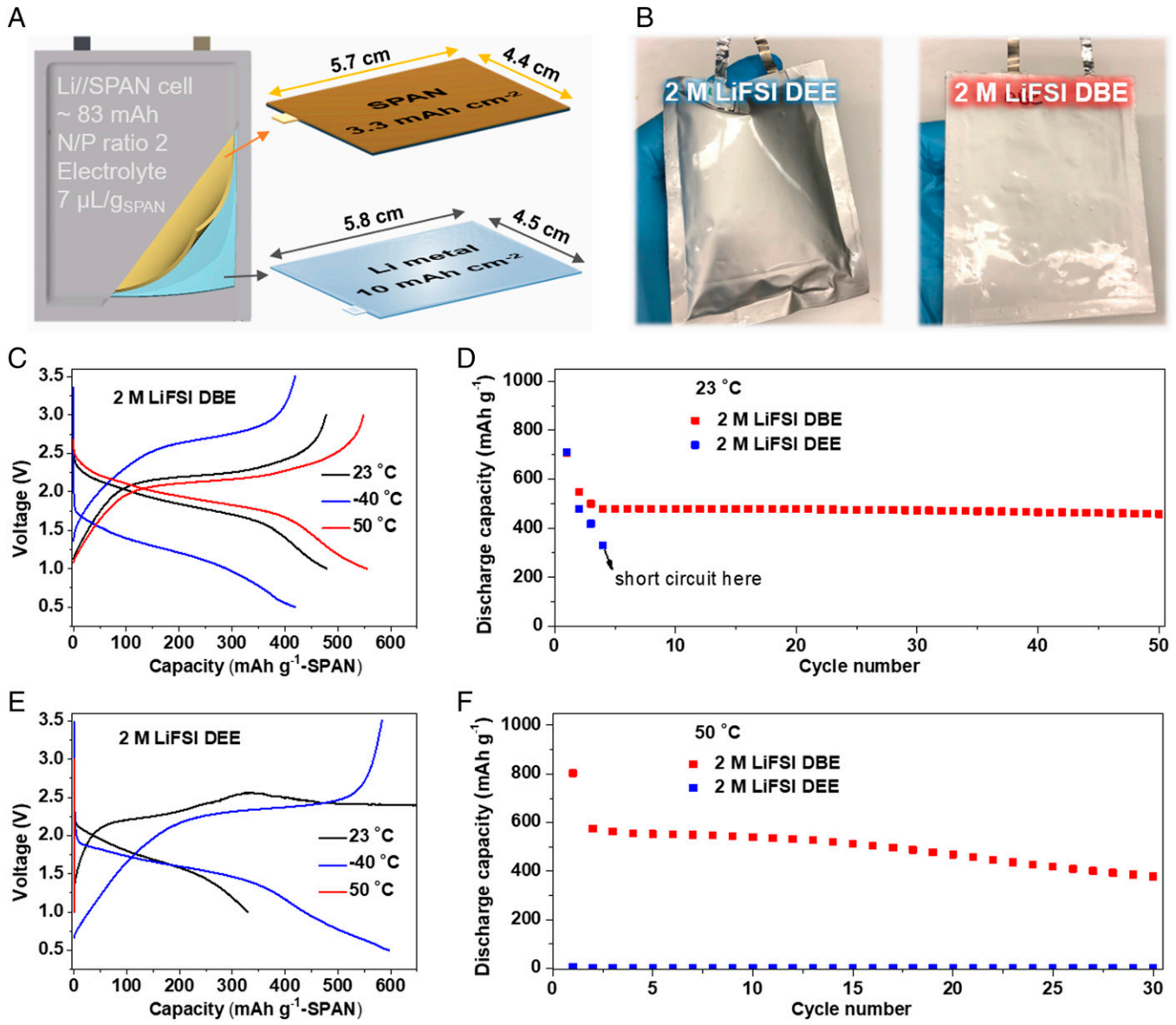

Fig. 5. Li–S pouch cell performance at a wide temperature range. (*A*) Schematic showing the assembly and parameter of the pouch cells. (*B*) Photographs of pouch cells with 2 M LiFSI DEE (*Left*) and 2 M LiFSI DBE (*Right*) after heating at 80 °C, in which a noticeable bulge can be found in the former. (*C*) Voltage curves of fourth cycle and (*D*) cycling performance of Li//SPAN pouch cells at 23 °C with a current density of 0.05 A g^{-1}. (*E*) Voltage curves of fourth cycle and (*F*) cycling performance of Li//SPAN pouch cells at 50 °C with a current density of 0.05 A g^{-1}.

dissembling CR-2032–type Li//Cu cells after the deposition of 4 mAh cm^{-2} Li in 0.5 mA cm^{-2}. In addition, the plated Li metal morphology in the Li//SPAN cells after the 10th charge at 50 °C was also analyzed to investigate the effects of the possible shuttling of soluble PS species on the anode. The Li//SPAN cells were activated at an ambient condition for 2 cycles and then 3 cycles at 50 °C with a low-current density of 0.1 A g^{-1} before running the long-term cycling test with 0.5 A g^{-1}. After being washed with DME solvent and dried at room temperature in an Ar-filled glovebox, the SEM images were collected by an FEI Quanta 250 SEM to characterize the morphology of the plated Li metal in the selected electrolyte systems.

The surface analysis of the delithiated SPAN cathodes obtained from the above cycled Li//SPAN cells without washing was identified by XPS spectra (Kratos Analytical, Kratos AXIS Supra), which were collected with a 300 mm × 700 mm spot size during acquisition using the Al anode source at 15 kV. A step size of 1.0 eV was used for the survey scans, followed by high-resolution scans (0.05 eV) for the O 1s, F 1s, C 1s, and S 2p regions. The C–C bond (284.6 eV) was selected as the reference to fit all peaks on the SPAN samples.

Ionic conductivity testing. The ionic conductivity testing was conducted based on a 2-electrode setup, where a PTFE washer was sandwiched by two stainless-steel spacers. The value of electrolytic conductivity is based on the following equation:

in which A and L are the area and thickness of the pore in PTFE washer and R is the resistance measured by EIS testing at different temperatures.

Electrochemical impedance testing. The EIS profiles were collected using an Autolab potentiostat with an AC amplitude of 10 mV. Before any testing at different temperatures, the Li//Cu and Li//SPAN cells were allowed to hold at the targeted temperature for at least 1 h.

Computational simulation. MD simulations were performed in a Large-scale Atomic/Molecular Massively Parallel Simulator (LAMMPS) using the OPLS-AA force field with the FSI molecules description from previous reports (49, 50). For the determination of the electrolyte structure, simulation boxes containing ~250 total molecules were constructed using various ratios of each component as dictated by the stoichiometry of each system. The charges of the FSI$^-$ (bis(-fluorosulfonyl)imide) and Li$^+$ were scaled to the high-frequency dielectric properties of the solvents present in each system according to the documented method (51).

To obtain the ground-state structure in each system, an initial energy minimization at 0 K (energy and force tolerances of 10^{-4}) was performed. Subsequently,

the system was slowly heated from 0 K to room temperature at a constant volume over 0.01 ns using a Langevin thermostat, with a damping parameter of 100 ps. This was followed by 5 cycles of quench-annealing dynamics to eliminate the persistence of any metastable states, where the temperature was slowly cycled between 298 K and 894 K with a ramp period of 0.025 ns followed by 0.1 ns of dynamics at either temperature extreme. All five anneal cycles thus took 1.25 ns total. Afterward, the above system was equilibrated at the constant temperature (298 K) at constant pressure (1 bar) (NpT ensemble) for 1.5 ns. We resolved stresses in the system isotropically using the Andersen barostat (pressure relaxation constant of 1 ps). Finally, we performed 10 ns of constant volume, constant temperature dynamics at 298 K. Radial distribution functions were collected using the Visual Molecular Dynamics (VMD) software. Pictures of the various solvation shells sampled from the simulation trajectory were also obtained using the VMD.

Coin and pouch cell assembly. For the Li//SPAN half-cells, CR-2032–type coin cells were assembled with SPAN cathodes (12 mm disk), the selected electrolyte (40 μL for 1.2 mAh cm^{-2} SPAN cathode), a Celgard 2325 membrane, and Li foils. For high-temperature and ultralow-temperature testing, Li//SPAN coin cells were activated at an ambient condition by running two cycles with 0.1 A g^{-1} and then were rested in freezers (−40 °C) or ovens (50 °C) for more than 2 h before galvanostatic cycling at extreme conditions.

For the pouch cells, the full cells with an N/P ratio of 2 were assembled with SPAN cathodes (5.7 cm * 4.4 cm, ∼3.3 mAh cm^{-2} SPAN), the selected electrolyte (∼7 μL $g_{SPAN}{}^{-1}$), Celgard 2325 membrane, and Li foils (10 mAh cm^{-2}). Two 6-in steel spring clamps with protective clips and a 2.5-in jaw opening were used to control the cell stack pressure (∼100 kPa).

Data Availability. All study data are included in the article, *SI Appendix*, and/or Movies S1 and S2.

ACKNOWLEDGMENTS. This work was supported by an Early Career Faculty grant from NASA's Space Technology Research Grants Program (ECF 80NSSC18K1512) (Z.C.). This research was partially supported by the NSF through the University of California San Diego (UCSD) Materials Research Science and Engineering Center, grant number DMR-2011924 (Z.C. and T.A.P.). This work was also supported by the Office of Vehicle Technologies of the U.S. Department of Energy through the Advanced Battery Materials Research Program (Battery500 Consortium) under contract number DE-EE0007764 (P.L.). The majority of the cell fabrication and electrochemical testing was performed in the UCSD-MTI Battery Fabrication and the UCSD-Arbin Battery Testing Facility. This work was performed in part at the San Diego Nanotechnology Infrastructure of UCSD, a member of the National Nanotechnology Coordinated Infrastructure, which is supported by the NSF (grant ECCS-1542148).

1. A. Gupta, A. Manthiram, Designing advanced lithium-based batteries for low-temperature conditions. *Adv. Energy Mater.* **10**, 2001972 (2020).
2. D. Luo *et al.*, Electrolyte design for lithium metal anode-based batteries toward extreme temperature application. *Adv. Sci. (Weinh.)* **8**, e2101051 (2021).
3. X. Dong *et al.*, High-energy rechargeable metallic lithium battery at -70°C enabled by a cosolvent electrolyte. *Angew. Chem. Int. Ed. Engl.* **58**, 5623–5627 (2019).
4. Q. Li *et al.*, Li^+-desolvation dictating lithium-ion battery's low-temperature performances. *ACS Appl. Mater. Interfaces* **9**, 42761–42768 (2017).
5. C. S. Rustomji *et al.*, Liquefied gas electrolytes for electrochemical energy storage devices. *Science* **356**, eaal4263 (2017).
6. M.-T. F. Rodrigues *et al.*, A materials perspective on Li-ion batteries at extreme temperatures. *Nat. Energy* **2**, 17108 (2017).
7. G. Cai *et al.*, Sub-nanometer confinement enables facile condensation of gas electrolyte for low-temperature batteries. *Nat. Commun.* **12**, 3395 (2021).
8. M. C. Smart *et al.*, The use of lithium-ion batteries for JPL's Mars missions. *Electrochim. Acta* **268**, 27–40 (2018).
9. X. Fan *et al.*, All-temperature batteries enabled by fluorinated electrolytes with non-polar solvents. *Nat. Energy* **4**, 882–890 (2019).
10. J. Wang *et al.*, Improving cyclability of Li metal batteries at elevated temperatures and its origin revealed by cryo-electron microscopy. *Nat. Energy* **4**, 664–670 (2019).
11. K. Yan *et al.*, Temperature-dependent nucleation and growth of dendrite-free lithium metal anodes. *Angew. Chem. Int. Ed. Engl.* **58**, 11364–11368 (2019).
12. C.-Y. Wang *et al.*, Lithium-ion battery structure that self-heats at low temperatures. *Nature* **529**, 515–518 (2016).
13. J. Liu *et al.*, Pathways for practical high-energy long-cycling lithium metal batteries. *Nat. Energy* **4**, 180–186 (2019).
14. X. Fan *et al.*, Non-flammable electrolyte enables Li-metal batteries with aggressive cathode chemistries. *Nat. Nanotechnol.* **13**, 715–722 (2018).
15. J. Zheng *et al.*, Regulating electrodeposition morphology of lithium: Towards commercially relevant secondary Li metal batteries. *Chem. Soc. Rev.* **49**, 2701–2750 (2020).
16. D. Lin, Y. Liu, Y. Cui, Reviving the lithium metal anode for high-energy batteries. *Nat. Nanotechnol.* **12**, 194–206 (2017).
17. Y. Zhang *et al.*, Towards better Li metal anodes: Challenges and strategies. *Mater. Today* **33**, 56–74 (2020).
18. Q. Pang, X. Liang, C. Y. Kwok, L. F. Nazar, Advances in lithium–sulfur batteries based on multifunctional cathodes and electrolytes. *Nat. Energy* **1**, 1–11 (2016).
19. Z. Du *et al.*, Cobalt in nitrogen-doped graphene as single-atom catalyst for high-sulfur content lithium–sulfur batteries. *J. Am. Chem. Soc.* **141**, 3977–3985 (2019).
20. W. G. Lim, S. Kim, C. Jo, J. Lee, A comprehensive review of materials with catalytic effects in Li–S batteries: Enhanced redox kinetics. *Angew. Chem. Int. Ed. Engl.* **58**, 18746–18757 (2019).
21. J. Zhang *et al.*, Nanostructured host materials for trapping sulfur in rechargeable Li-S batteries: structure design and interfacial chemistry. *Small Methods* **2**, 1700279 (2018).
22. J. Zhang, Z. Li, Y. Chen, S. Gao, X. W. D. Lou, Nickel–iron layered double hydroxide hollow polyhedrons as a superior sulfur host for lithium–sulfur batteries. *Angew. Chem. Int. Ed. Engl.* **57**, 10944–10948 (2018).
23. Y. Liu, P. He, H. Zhou, Rechargeable solid-state Li-air and Li–S batteries: Materials, construction, and challenges. *Adv. Energy Mater.* **8**, 1701602 (2018).
24. H.-S. Ryu *et al.*, Discharge behavior of lithium/sulfur cell with TEGDME based electrolyte at low temperature. *J. Power Sources* **163**, 201–206 (2006).
25. J.-Q. Huang *et al.*, Entrapment of sulfur in hierarchical porous graphene for lithium-sulfur batteries with high rate performance from -40 to 60°C. *Nano Energy* **2**, 314–321 (2013).
26. G. Cai *et al.*, An ester electrolyte for lithium-sulfur batteries capable of ultra-low temperature cycling. *Chem. Commun. (Camb.)* **56**, 9114–9117 (2020).
27. A. Gupta, A. Bhargav, J.-P. Jones, R. V. Bugga, A. Manthiram, Influence of lithium polysulfide clustering on the kinetics of electrochemical conversion in lithium-sulfur batteries. *Chem. Mater.* **32**, 2070–2077 (2020).
28. Y. V. Mikhaylik, J. R. Akridge, Low temperature performance of Li/S batteries. *J. Electrochem. Soc.* **150**, A306 (2003).
29. J. Holoubek *et al.*, Tailoring electrolyte solvation for Li metal batteries cycled at ultra-low temperature. *Nat. Energy* **2021**, 303–313 (2021).
30. Z. Zhou, G. Li, J. Zhang, Y. Zhao, Wide working temperature range rechargeable lithium–sulfur batteries: a critical review. *Adv. Funct. Mater.* **31**, 2107136 (2021).
31. C. Luo *et al.*, A chemically stabilized sulfur cathode for lean electrolyte lithium sulfur batteries. *Proc. Natl. Acad. Sci. U.S.A.* **117**, 14712–14720 (2020).
32. R. Fang, J. Xu, D.-W. Wang, Covalent fixing of sulfur in metal-sulfur batteries. *Energy Environ. Sci.* **13**, 432–471 (2020).
33. W. J. Chen *et al.*, Electrolyte regulation towards stable lithium-metal anodes in lithium-sulfur batteries with sulfurized polyacrylonitrile cathodes. *Angew. Chem. Int. Ed. Engl.* **59**, 10732–10745 (2020).
34. X. Chen *et al.*, Ether-compatible sulfurized polyacrylonitrile cathode with excellent performance enabled by fast kinetics via selenium doping. *Nat. Commun.* **10**, 1021 (2019).
35. S. Wei, L. Ma, K. E. Hendrickson, Z. Tu, L. A. Archer, Metal-sulfur battery cathodes based on PAN-sulfur composites. *J. Am. Chem. Soc.* **137**, 12143–12152 (2015).
36. H. Yang, J. Chen, J. Yang, J. Wang, Prospect of sulfurized pyrolyzed poly (acrylonitrile)(S@pPAN) cathode materials for rechargeable lithium batteries. *Angew. Chem. Int. Ed. Engl.* **59**, 7306–7318 (2020).
37. C. Yan *et al.*, An armored mixed conductor interphase on a dendrite-free lithium-metal anode. *Adv. Mater.* **30**, e1804461 (2018).
38. C. Fu *et al.*, Correlating Li^+-solvation structure and its electrochemical reaction kinetics with sulfur in subnano confinement. *J. Phys. Chem. Lett.* **9**, 1739–1745 (2018).
39. X. Zhang, A. Wang, X. Liu, J. Luo, Dendrites in lithium metal anodes: suppression, regulation, and elimination. *Acc. Chem. Res.* **52**, 3223–3232 (2019).
40. W. A. Henderson, Glyme-lithium salt phase behavior. *J. Phys. Chem. B* **110**, 13177–13183 (2006).
41. L. Carbone *et al.*, Comparative study of ether-based electrolytes for application in lithium-sulfur battery. *ACS Appl. Mater. Interfaces* **7**, 13859–13865 (2015).
42. Y. Tsao *et al.*, Designing a quinone-based redox mediator to facilitate Li_2S oxidation in Li-S batteries. *Joule* **3**, 872–884 (2019).
43. G. Li *et al.*, Organosulfide-plasticized solid-electrolyte interphase layer enables stable lithium metal anodes for long-cycle lithium-sulfur batteries. *Nat. Commun.* **8**, 850 (2017).
44. A. C. Thenuwara *et al.*, Efficient low-temperature cycling of lithium metal anodes by tailoring the solid-electrolyte interphase. *ACS Energy Lett.* **5**, 2411–2420 (2020).
45. B. D. Adams, J. Zheng, X. Ren, W. Xu, J. G. Zhang, Accurate determination of Coulombic efficiency for lithium metal anodes and lithium metal batteries. *Adv. Energy Mater.* **8**, 1702097 (2018).
46. Y. Yamada, J. Wang, S. Ko, E. Watanabe, A. Yamada, Advances and issues in developing salt-concentrated battery electrolytes. *Nat. Energy* **4**, 269–280 (2019).
47. E. R. Logan, J. R. Dahn, Electrolyte design for fast-charging Li-ion batteries. *Trends Chem.* **2**, 354–366 (2020).
48. J. Qian *et al.*, High rate and stable cycling of lithium metal anode. *Nat. Commun.* **6**, 6362 (2015).
49. G. A. Kaminski, R. A. Friesner, J. Tirado-Rives, W. L. Jorgensen, Evaluation and reparametrization of the OPLS-AA force field for proteins via comparison with accurate quantum chemical calculations on peptides. *J. Phys. Chem. B* **105**, 6474–6487 (2001).
50. A. S. L. Gouveia *et al.*, Ionic liquids with anions based on fluorosulfonyl derivatives: from asymmetrical substitutions to a consistent force field model. *Phys. Chem. Chem. Phys.* **19**, 29617–29624 (2017).
51. C. Park *et al.*, Molecular simulations of electrolyte structure and dynamics in lithium–sulfur battery solvents. *J. Power Sources* **373**, 70–78 (2018).